BULLETIN OF THE POLISH ACADEMY OF SCIENCES
TECHNICAL SCIENCES, Vol. 71(6), 2023, Article number: e148252
DOI: 10.24425/bpasts.2023.148252

SPECIAL SECTION

Efficient rotordynamic simulations with semi-analytical computation of hydrodynamic forces

Simon PFEIL*, Fabian DUVIGNEAU, and Elmar WOSCHKE

Otto von Guericke University, Institute of Mechanics, Universitätspl. 2, 39106 Magdeburg, Germany

Abstract. A common problem in transient rotordynamic simulations is the numerical effort necessary for the computation of hydrodynamic bearing forces. Due to the nonlinear interaction between the rotordynamic and hydrodynamic systems, an adequate prediction of shaft oscillations requires a solution of the Reynolds equation at every time step. Since closed-form analytical solutions are only known for highly simplified models, numerical methods or look-up table techniques are usually employed. Numerical solutions provide excellent accuracy and allow a consideration of various physical influences that may affect the pressure generation in the bearing (e.g., cavitation or shaft tilting), but they are computationally expensive. Look-up tables are less universal because the interpolation effort and the database size increase significantly with every considered physical effect that introduces additional independent variables. In recent studies, the Reynolds equation was solved semi-analytically by means of the scaled boundary finite element method (SBFEM). Compared to the finite element method (FEM), this solution is relatively fast if a small discretization error is desired or if the slenderness ratio of the bearing is large. The accuracy and efficiency of this approach, which have already been investigated for single calls of the Reynolds equation, are now examined in the context of rotordynamic simulations. For comparison of the simulation results and the computational effort, two numerical reference solutions based on the FEM and the finite volume method (FVM) are also analyzed.

Key words: SBFEM; Reynolds equation; hydrodynamic bearings; rotordynamics.

1. INTRODUCTION

As a fundamental component of various types of rotor systems, hydrodynamic bearings provide excellent load and damping capacities and wear behavior. However, their nonlinear characteristics often lead to undesired oscillations (oil whirl and whip [1, 2]) in high-speed rotor systems, which may cause critical noise emissions, reduce the energy efficiency of the machine, or even damage the components. Moreover, the nonlinear interaction between the rotor and the bearing complicates the prediction of the operating behavior in the product development process. Transient simulations with detailed modeling of the coupled rotordynamic and hydrodynamic systems as well as precise knowledge of the boundary conditions (BCs) are necessary. Due to the nonlinear coupling of the two systems, these simulations have to be performed in the time domain, based on time integration schemes [2]. The hydrodynamic forces, governed by the Reynolds equation, are computed at every time step under consideration of the current kinematic variables of the bearing partners. These forces are then applied to the bodies in their equations of motion.

The Reynolds equation [3] describes the pressure generation in narrow fluid films and is classified as a second-order partial differential equation. Exact, closed-form solutions are only known for the theoretical special cases of infinitely long [4] or infinitesimally short [5] bearings. For realistic bearings with general BCs and arbitrary gap geometries, an adequate accuracy is achieved by means of numerical methods, typically the finite element method (FEM) [6, 7], the finite volume method (FVM) [8], or the finite difference method (FDM) [9]. Since the equation is solved at every time step, the resulting computational effort can be problematic. A common alternative is the look-up table technique, which is based on the interpolation of pre-computed data points [10, 11]. However, the modeling depth of this approach is limited, since the amount of data and the interpolation effort increase substantially with every considered physical effect. Numerical models, on the other hand, can be extended to consider shaft tilting [12], mass-conserving cavitation [13, 14], elasto-hydrodynamics [15, 16], thermo-hydrodynamics [17], or hydraulic coupling of oil films [18].

In recent studies [19–21], the Reynolds equation was solved semi-analytically by means of the scaled boundary finite element method (SBFEM) with the objective of reducing the computational effort in comparison to the standard numerical methods while maintaining their accuracy. The SBFEM was originally developed for wave propagation problems in unbounded domains [22, 23] and has since then been adopted in other fields, for example, fracture analysis [24, 25]. For the SBFEM solution of the Reynolds equation, the bearing is discretized only in the circumferential direction, whereas in the axial direction, an exact analytical formulation is used. In [19, 20], it was ob-

*e-mail: simon.pfeil@ovgu.de

Manuscript submitted 2023-05-04, revised 2023-11-01, initially accepted for publication 2023-11-01, published in December 2023.

© 2023 The Author(s). This is an open access article under the CC BY license (http://creativecommons.org/licenses/by/4.0/)

served that the efficiency of this approach, relative to the FEM, depends on the slenderness ratio $\varsigma = l/d$ (bearing length l divided by diameter d), the oil supply BCs, and the discretization. The SBFEM is relatively efficient if the slenderness ratio is large ($\varsigma > 1.5$), if the bearing is modeled without (or only simplified) oil supply BCs, or if a fine discretization (large node number or high-order interpolation) is desired. In [21], the SBFEM solution was combined with an advanced cavitation model but, so far, only under quasi-static conditions.

In previous studies on the SBFEM solution of the Reynolds equation, the efficiency of the method was only investigated for single calls of the algorithm and always in comparison to either the FEM or the FVM. In the study at hand, all three approaches (SBFEM, FEM, and FVM) are compared to each other on the basis of time integrations, where the Reynolds equation is solved at every step. As far as cavitation is concerned, all simulations in this study are still performed under Gümbel conditions [26] (highly simplified, but fast handling of cavitation) because the SBFEM algorithm that is able to consider this effect in a more sophisticated manner (see [21]) has not been extended to the transient case yet.

2. THEORY

2.1. Equation of motion

The rotordynamic model for this study is implemented in a multibody system (MBS) program with custom force routines for the hydrodynamic bearings. The equation of motion can be written as [2]

$$\underline{\underline{M}} \cdot \ddot{\underline{s}} + \underline{F}_\omega = \underline{F}_{\text{out}}\,, \tag{1}$$

where $\underline{s}$ contains the body positions and orientations, $\underline{\underline{M}}$ is the mass matrix, and $\underline{F}_\omega$ is the vector of centrifugal, gyroscopic, and coriolis forces. The vector $\underline{F}_{\text{out}}$ contains the external forces due to, e.g., gravitation, springs, dampers, or bearings. Equation (1) is solved by means of numerical time integration based on the trapezoidal rule. More specifically, Matlab's ODE23t-solver[1] [27] is used, which requires a first-order formulation of the second-order differential equation (1)

$$\begin{bmatrix} \underline{\underline{\mathrm{I}}} & \underline{\underline{0}} \\ \underline{\underline{0}} & \underline{\underline{M}} \end{bmatrix} \cdot \dot{\underline{z}} = \begin{bmatrix} \dot{\underline{s}} \\ \underline{F}_{\text{out}} - \underline{F}_\omega \end{bmatrix} \quad \text{with} \quad \underline{z} = \begin{bmatrix} \underline{s} \\ \dot{\underline{s}} \end{bmatrix}, \tag{2}$$

where $\underline{\underline{\mathrm{I}}}$ is the identity matrix.

2.2. Reynolds equation

For hydrodynamic journal bearings (Fig. 1a) with constant oil viscosity μ and density ρ, the Reynolds equation [3] can be written as

$$\frac{1}{12\mu r^2}(h^3 p_{,\theta})_{,\theta} + \frac{1}{12\mu}(h^3 p_{,y})_{,y} = \frac{\omega_{\text{rot}}}{2} h_{,\theta} + \dot{h}, \tag{3}$$

where the pressure $p(\theta, y, t)$ is the dependent variable, θ and y are the circumferential and axial coordinates, respectively, $r = d/2$ is the bearing radius, and ω_{rot} is the rotational velocity (angular frequency) of the shaft. The gap function $h(\theta, t)$ describes the gap width between the bearing partners and is given as

$$h = c - q\cos(\theta - \theta_{\text{att}}) \tag{4}$$

for cylindrical bearings under negligence of shaft tilting. Here, c is the clearance, $q(t)$ is the eccentricity, and $\theta_{\text{att}}(t)$ is the attitude angle. Note that q and θ_{att} can be derived from the state vector of the shaft at every time step, which means that the gap function h is also explicitly known. The same applies to their time derivatives $\dot{q}(t)$ and $\dot{\theta}_{\text{att}}(t)$ and, hence, also to the function $\dot{h}(\theta, t)$.

The computational domain can be pictured as a rectangle representing the unwinded lubrication gap (Fig. 1b), with the two bearing boundaries located at $y = \pm l/2$ as well as two periodic boundaries at $\theta = 0$ and $\theta = 2\pi$. However, since shaft tilting is neglected in this study ($h_{,y} = 0$), the resulting pressure field is symmetric, which will be exploited in all computational models (SBFEM, FEM, and FVM) by means of a symmetric BC. This allows a reduction of the computational domain to one half of the original axial range, that is[2], $0 \le y \le l/2$. At the bearing boundary, a Dirichlet BC is enforced that prescribes atmospheric pressure[3], i.e., $p(\theta, y = l/2, t) = 0$. Oil supply BCs will not be considered in this study.

For the purpose of reducing the condition numbers of the equation systems, equation (3) is nondimensionalized. This is achieved by means of the substitutions

$$p = P\frac{6r^2\mu\omega_{\text{rot}}}{c^2}\,, \quad h = Hc\,, \quad y = Yr, \tag{5}$$

where P is the dimensionless pressure, H is the dimensionless gap function, and Y is the dimensionless axial coordinate[4], leading to the dimensionless Reynolds equation

$$(H^3 P_{,\theta})_{,\theta} + (H^3 P_{,Y})_{,Y} = H_{,\theta} + \frac{2}{\omega_{\text{rot}}}\dot{H}\,. \tag{6}$$

After the solution of this equation (by means of the SBFEM, FEM, or FVM), the Gümbel approach [26] is employed for simplified (but fast) handling of cavitation, that is, all negative pressures are artificially set to zero (since $p_{\text{cav}} \approx p_{\text{atm}} = 0$,

[1] ODE = ordinary differential equation.

[2] With shaft tilting, the SBFEM equation (13) becomes more complicated and its analytical solution is no longer obvious. Mathematical strategies that may provide an approximate solution under these conditions will be investigated in future studies. In the study at hand, shaft tilting is neglected in all simulation models, including also the numerical reference solutions (FEM and FVM). In general, the FEM and FVM can be formulated to consider this effect, but the computational effort increases in that case as the symmetric BC cannot be used. Note that the negligence of shaft tilting in the bearing model does not prevent the occurrence of shaft tilting in the rotordynamic or multibody system; it only means that the effect of this tilting motion on the pressure generation is ignored.

[3] Relative pressures are used, which means that atmospheric pressure is defined as zero.

[4] Note that in Fig. 1b, the location of the bearing boundary ($y = l/2$) is expressed with respect to the dimensionless coordinate $Y = y/r$ by the slenderness ratio ς, since $Y(y = l/2) = (l/2)/r = l/d = \varsigma$.

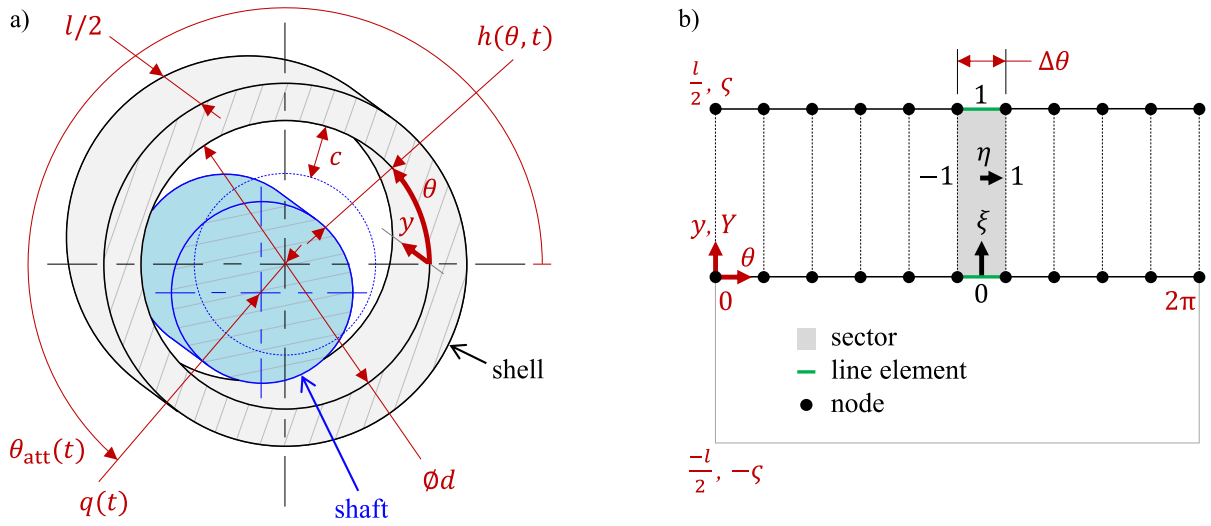

Fig. 1. a) Sketch of one half of a hydrodynamic bearing (with exaggerated clearance), consisting of a rotating shaft (blue and turquoise), a fixed shell (black and gray), and a lubrication gap in between. b) Computational domain of the Reynolds equation (unwinded lubrication gap) with SBFEM model

where p_{cav} represents cavitation pressure). The resulting pressure field is then integrated over the shaft surface for the computation of the bearing force vector

$$\underline{F}_{\text{b}} = -r \int_0^{2\pi} \int_{-l/2}^{l/2} p \begin{bmatrix} \cos(\theta) \\ \sin(\theta) \end{bmatrix} \mathrm{d}y \mathrm{d}\theta, \tag{7}$$

which is incorporated into $\underline{F}_{\text{out}}$ for the equation of motion (1).

2.2.1. SBFEM solution

In the SBFEM model (Fig. 1b), the computational domain is subdivided into an equidistant grid of sectors in the circumferential direction (the gray area represents an exemplary sector e). Within the sector, the dependent variable P is expressed by a semi-analytical ansatz

$$P_{\text{e}}(\eta, \xi) = \underline{N}^{\text{T}}(\eta) \cdot \underline{P}_{\text{e}}(\xi), \tag{8}$$

where $\{\eta, \xi\}$ is a local coordinate system (with η as circumferential and ξ as axial coordinate) and $\underline{N}(\eta)$ is a vector of shape functions. The vector $\underline{P}_{\text{e}}(\xi)$ contains the nodal solutions, but rather than discrete values, these are functions of the axial coordinate ξ (no assumption as to the type of function is made at this point). Hence, only the circumferential direction is discretized.

The Galerkin method [7] is applied to the Reynolds equation (6), leading to the weak form

$$\int_0^{\varsigma} \int_0^{2\pi} W \Big[(H^3 P_{,\theta})_{,\theta} + (H^3 P_{,Y})_{,Y} - H_{,\theta} - \frac{2}{\omega_{\text{rot}}} \dot{H} \Big] \mathrm{d}\theta \mathrm{d}Y = 0, \tag{9}$$

where W is a test function. Equation (9) is transformed into the local coordinate system of the sector, and the ansatz defined in equation (8) is applied. After a few further steps described in [19], this leads to a system of ordinary differential equations for every sector

$$\underline{\underline{E}}_{0_{\text{e}}} \cdot \underline{P}_{\text{e},\xi\xi}(\xi) - \underline{\underline{E}}_{2_{\text{e}}} \cdot \underline{P}_{\text{e}}(\xi) = \underline{R}_{\text{e}} \tag{10}$$

with

$$\underline{\underline{E}}_{0_{\text{e}}} = \frac{\Delta\theta}{2\varsigma^2} \int_{-1}^{1} H^3 \underline{N} \cdot \underline{N}^{\text{T}} \mathrm{d}\eta, \quad \underline{\underline{E}}_{2_{\text{e}}} = \frac{2}{\Delta\theta} \int_{-1}^{1} H^3 \underline{N}_{,\eta} \cdot \underline{N}_{,\eta}^{\text{T}} \mathrm{d}\eta,$$

$$\underline{R}_{\text{e}} = \int_{-1}^{1} H_{,\eta} \underline{N} \mathrm{d}\eta + \frac{\Delta\theta}{\omega_{\text{rot}}} \int_{-1}^{1} \dot{H} \underline{N} \mathrm{d}\eta, \tag{11}$$

where $\Delta\theta$ is the circumferential sector length. The solution of the integrals in equation (11) is performed analytically because only linear shape functions are used in this study[5]. The integration is further facilitated by means of the approximations

$$H = \frac{H_{\text{n1}} + H_{\text{n2}}}{2}, \quad \dot{H} = \frac{\dot{H}_{\text{n1}} + \dot{H}_{\text{n2}}}{2}, \quad H_{,\eta} = \frac{H_{\text{n2}} - H_{\text{n1}}}{2}, \tag{12}$$

where the gap function is only evaluated at the two circumferential nodal positions of the sector. These positions are indicated by $(\cdot)_{\text{n1}}$ (at $\eta = -1$) and $(\cdot)_{\text{n2}}$ (at $\eta = 1$), respectively. The matrices and the vector defined in equation (11) are assembled over all sectors, so that equation (10) can be expressed globally as

$$\underline{\underline{E}}_0 \cdot \underline{P}_{,\xi\xi}(\xi) - \underline{\underline{E}}_2 \cdot \underline{P}(\xi) = \underline{R}. \tag{13}$$

[5]Future investigations similar to this study will be performed under consideration of higher-order shape functions. For the paper at hand, this would increase the scope of content too far.

The solution of this equation can be written as the sum of a homogeneous and a particular solution [19]

$$\underline{P}(\xi) = \underline{P}_{\text{hom}}(\xi) + \underline{P}_{\text{par}} \tag{14}$$

with

$$\begin{aligned} \underline{P}_{\text{par}} &= -\underline{\underline{E}}_2^{-1} \cdot \underline{R}, \\ \underline{P}_{\text{hom}}(\xi) &= \underline{\underline{\hat{P}}} \cdot (\cosh \underline{\underline{\Lambda}})^{-1} \cdot \cosh(\xi \underline{\underline{\Lambda}}) \cdot \underline{C}, \end{aligned} \tag{15}$$

where $\underline{\underline{\hat{P}}}$ is a matrix of eigenvectors and $\underline{\underline{\Lambda}}$ a diagonal matrix of eigenvalues obtained from the solution of the generalized eigenvalue problem [19]

$$\underline{\underline{E}}_2 \cdot \underline{\underline{\hat{P}}} = \underline{\underline{E}}_0 \cdot \underline{\underline{\hat{P}}} \cdot \underline{\underline{\Lambda}}^2 . \tag{16}$$

The vector $\underline{C}$ in equation (15) contains the integration constants of the homogeneous solution, which depend on the BCs at the bearing boundary. These BCs are enforced by means of the equation system [19]

$$\underline{C} = -\underline{\underline{\hat{P}}}^{-1} \cdot \underline{P}_{\text{par}} . \tag{17}$$

2.2.2. FEM reference solution

The FEM [28] model[6] uses a two-dimensional, regular grid of quadrilateral four-node elements. In every element e, the dependent variable P is expressed as

$$P_{\text{e}}(\eta, \psi) = \underline{N}^{\text{T}}(\eta, \psi) \cdot \underline{P}_{\text{e}}, \tag{18}$$

where $\{\eta, \psi\}$ is a local coordinate system and $\underline{P}_{\text{e}}$ is a vector of discrete nodal solutions that are interpolated in both directions by a vector of shape functions $\underline{N}(\eta, \psi)$. Analogously to the SBFEM, the weak form given in equation (9) is used, but in combination with the ansatz defined in equation (18), a linear equation system

$$\underline{\underline{K}}_{\text{e}} \cdot \underline{P}_{\text{e}} = \underline{R}_{\text{e}} \tag{19}$$

with

$$\begin{aligned} \underline{\underline{K}}_{\text{e}} &= \frac{\Delta Y}{\Delta \theta} \int_{-1}^{1} \int_{-1}^{1} H^3 \underline{N}_{,\eta} \cdot \underline{N}_{,\eta}^{\text{T}} \, \mathrm{d}\eta \, \mathrm{d}\psi \\ &\quad + \frac{\Delta \theta}{\Delta Y} \int_{-1}^{1} \int_{-1}^{1} H^3 \underline{N}_{,\psi} \cdot \underline{N}_{,\psi}^{\text{T}} \, \mathrm{d}\eta \, \mathrm{d}\psi , \\ \underline{R}_{\text{e}} &= -\frac{\Delta Y}{2} \int_{-1}^{1} \int_{-1}^{1} H_{,\eta} \underline{N} \, \mathrm{d}\eta \, \mathrm{d}\psi - \frac{\Delta \theta \Delta Y}{2 \omega_{\text{rot}}} \int_{-1}^{1} \int_{-1}^{1} \dot{H} \underline{N} \, \mathrm{d}\eta \, \mathrm{d}\psi \end{aligned} \tag{20}$$

is obtained, where $\Delta\theta$ and ΔY are the circumferential and axial element length, respectively. Analogously to the SBFEM model, only linear shape functions are used and the gap function H as well as its derivatives are approximated in a similar manner to equation (12), allowing a straightforward analytical integration. The assembly of equation (20) over all elements yields a global linear equation system

$$\underline{\underline{K}} \cdot \underline{P} = \underline{R} . \tag{21}$$

The Dirichlet BCs at the bearing boundary are enforced by elimination of the respective equations and degrees of freedom from equation (21) before the equation system is solved.

2.2.3. FVM reference solution

In the FVM [29] model, the computational domain is subdivided into a two-dimensional, regular grid of quadrilateral control volumes[7], each containing one node at its center. For this regular grid, the FVM leads to the same matrices as the FDM, which is why the FDM will not be investigated separately in this study. The FVM formulation is based on a weak form obtained by integration of the Reynolds equation (6) over the control volume

$$\begin{aligned} &\int_{Y_1}^{Y_2} \int_{\theta_1}^{\theta_2} \left[(H^3 P_{,\theta})_{,\theta} + (H^3 P_{,Y})_{,Y} \right] \mathrm{d}\theta \, \mathrm{d}Y \\ &\quad = \int_{Y_1}^{Y_2} \int_{\theta_1}^{\theta_2} \left[H_{,\theta} + \frac{2}{\omega_{\text{rot}}} \dot{H} \right] \mathrm{d}\theta \, \mathrm{d}Y , \end{aligned} \tag{22}$$

where $\theta_1 \leq \theta \leq \theta_2$ and $Y_1 \leq Y \leq Y_2$ represent the circumferential and axial range of the control volume, respectively. After some analytical integration, equation (22) can be written as

$$\begin{aligned} &\int_{Y_1}^{Y_2} (H^3 P_{,\theta})_{\theta_2} - (H^3 P_{,\theta})_{\theta_1} \mathrm{d}Y + \int_{\theta_1}^{\theta_2} (H^3 P_{,Y})_{Y_2} - (H^3 P_{,Y})_{Y_1} \mathrm{d}\theta \\ &\quad = \int_{Y_1}^{Y_2} H_{\theta_2} - H_{\theta_1} \mathrm{d}Y + \frac{2}{\omega_{\text{rot}}} \int_{Y_1}^{Y_2} \int_{\theta_1}^{\theta_2} \dot{H} \, \mathrm{d}\theta \, \mathrm{d}Y \end{aligned} \tag{23}$$

with the indices θ_1, θ_2, Y_1, and Y_2 specifying where the functions in parentheses are evaluated. Hence, the first three terms of equation (23) describe an integration over the control volume boundaries and the fourth term an integration over the control volume. For the former case (integration over the boundaries), one integration point is defined at the center of each of the four control volume boundaries. Here, the functions $P_{,\theta}$, $P_{,Y}$, and H are evaluated based on linear interpolations of P and H between the node at the center of the control volume (which will be denoted as 0) and the four neighboring nodes (which will be denoted as N, E, S, and W)[8]. For $\dot{H}$, a single integration point at node 0 is defined. Hence, every term

[6] This model is not depicted graphically because the FEM is a standard method. The same applies to the FVM model in Section 2.2.3.

[7] Mathematically, the Reynolds equation describes a two-dimensional problem (because the pressure is assumed to be constant in the gap width direction), but nonetheless, the conventional term control *volume* will be used.

[8] E and W are the neighboring nodes in the positive and negative θ-direction, respectively. N and S are the neighboring nodes in the positive and negative Y-direction, respectively.

in the integrals in equation (23) is approximated by a discrete value at an integration point, which simplifies the integration to

$$\int_{\theta_1}^{\theta_2} \mathrm{d}\theta = \Delta\theta\,, \quad \int_{Y_1}^{Y_2} \mathrm{d}Y = \Delta Y\,, \tag{24}$$

where $\Delta\theta$ and ΔY are the circumferential and axial control volume side lengths. equation (23) becomes

$$\begin{aligned}(a_\mathrm{N}+a_\mathrm{E}+a_\mathrm{S}+a_\mathrm{W})P_0 - a_\mathrm{N}P_\mathrm{N} - a_\mathrm{E}P_\mathrm{E} - a_\mathrm{S}P_\mathrm{S} - a_\mathrm{W}P_\mathrm{W} \\ = -\frac{\Delta Y}{2}(H_\mathrm{E}-H_\mathrm{W}) - \frac{2}{\omega_\mathrm{rot}}\Delta\theta\Delta Y\dot{H}_0\end{aligned} \tag{25}$$

with

$$\begin{aligned} a_\mathrm{N/S} &= \frac{1}{8}\frac{\Delta\theta}{\Delta Y}\left(H_0+H_\mathrm{N/S}\right)^3, \\ a_\mathrm{E/W} &= \frac{1}{8}\frac{\Delta Y}{\Delta\theta}\left(H_0+H_\mathrm{E/W}\right)^3. \end{aligned} \tag{26}$$

This equation is evaluated in all control volumes except for those at the bearing boundary, where the Dirichlet BC $P_0 = 0$ is prescribed. Thereby, a linear equation system is obtained[9]

$$\underline{\underline{K}} \cdot \underline{P} = \underline{R}. \tag{27}$$

3. COMPARISON OF SOLUTION TECHNIQUES

In this section, the SBFEM is compared to the FEM and the FVM by means of run-up simulations of a simple Laval rotor with hydrodynamic bearings (Fig. 2). The shaft is assumed to be massless except for a point mass m_1 with an unbalance u at the center and two point masses m_2 located at both ends of the rotor, that is, inside the two bearings. Due to the overall symmetry (indicated by the dashed line), only one bearing and one half of the rotor need to be simulated, which means that m_1 and u are also halved in the final implementation. The elastic shaft is modeled as a parallel spring-damper arrangement that couples the bodies m_1 and m_2 in the β_2- and γ_2-directions (body-fixed coordinate system of m_2) by means of the stiffness and damping coefficients k and b. Over the course of the simulation, the rotational velocity ω_rot is increased at a constant rate from ω_start to ω_end within the run-up time t_run.

Note that this particular setup has not been chosen with the objective to resemble a realistic machine but to reproduce in their simplest form the most fundamental oscillation phenomena in rotor systems with hydrodynamic bearings, namely an oil whip and an unbalance-induced vibration passing through a resonance. Due to the assumption of a massless shaft in combination with the overall symmetry (and because tilting of m_2 is prohibited for the sake of simplicity), the translations of m_1 and m_2 perpendicular to the rotation axis are the only degrees of freedom participating in the oscillation. Gyroscopic effects, asymmetric modes, and higher-order bending modes are not present. This simple academic example should suffice for the first comparison of the SBFEM to the FEM and FVM in a time integration, but in future studies, realistic technical systems will also be considered.

In Table 1, the parameters of the rotor system are summarized. The simulation is performed multiple times with different computational methods for the Reynolds equation (SBFEM, FEM, and FVM) and for different discretizations (different circumferential node numbers n_θ). The axial node number in the FEM and FVM is chosen in such a way that the side length of the elements or control volumes is almost identical in both directions (whereas the SBFEM requires no discretization in the axial direction). The eigenvalue problem in the SBFEM (equation (16)) and the equation systems in the FEM (equation (21)) and FVM (equation (27)), which dominate the numerical effort of the respective computational methods, are solved with Matlab's *eig* and *mldivide* commands, respectively. The automatically chosen algorithms under consideration of the given matrix properties[10] are in both cases based on Cholesky factorization [30]. All simulations are performed on a desktop PC (Intel(R) Core(TM) i7-8700 CPU, 3.2 GHz; 64 GB RAM) in Matlab R2019a.

Table 1
Parameters for the run-up simulations of the Laval rotor in Fig. 2

parameter	value	unit
b	1000	$\mathrm{N\cdot s/m}$
c	150	µm
d	0.1	m
g	9.81	$\mathrm{m/s^2}$
k	$4\cdot 10^7$	N/m
l	0.1	m
m_1	400	kg
m_2	1	kg
t_run	2	s
u	0.04	$\mathrm{kg\cdot m}$
μ	0.01	$\mathrm{Pa\cdot s}$
ω_start	$5\cdot 2\pi$	rad/s
ω_end	$200\cdot 2\pi$	rad/s

In Fig. 3a and Fig. 3b, some exemplary simulation results for the SBFEM model with the finest investigated discretization ($n_\theta = 480$) are displayed[11]. The former shows a spectrogram of the vertical shaft oscillations inside the bearing (vertical oscillations of the body m_2 in Fig. 2), where a and f are the amplitude and frequency of the vibration, respectively, and $f_\mathrm{rot} = \omega_\mathrm{rot}/(2\pi)$ is the rotational frequency of the shaft.

[9] Although this equation uses the same symbols as equation (21), the matrix $\underline{\underline{K}}$ may differ between the FEM and the FVM (cf. Section 3).

[10] The matrices $\underline{\underline{E}}_0$ and $\underline{\underline{E}}_2$ in the SBFEM as well as the matrix $\underline{\underline{K}}$ in the FEM or FVM are symmetric. Moreover, $\underline{\underline{E}}_0$ and $\underline{\underline{K}}$ are positive definite. All matrices are banded, but only $\underline{\underline{K}}$ is stored in sparse format (this matrix is a lot larger than $\underline{\underline{E}}_0$ and $\underline{\underline{E}}_2$).

[11] The results of the other simulations are qualitatively similar.

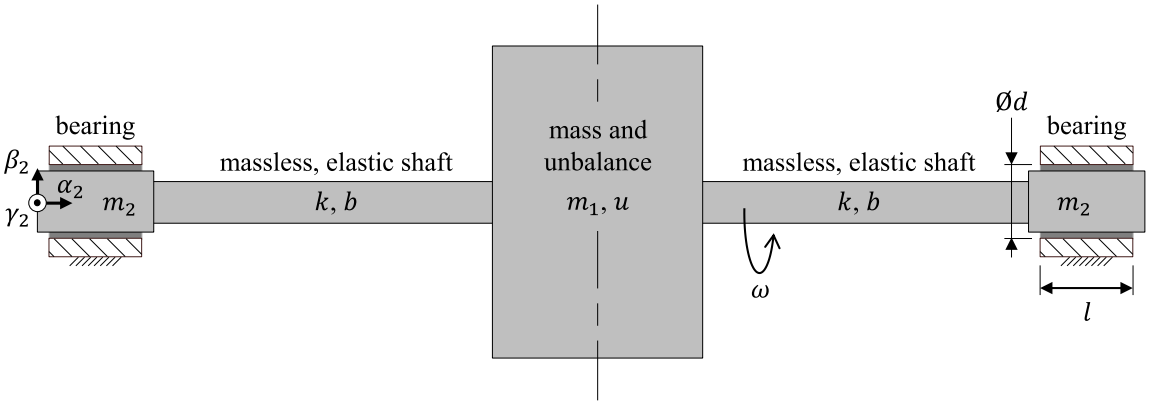

Fig. 2. Laval rotor with hydrodynamic bearings for exemplary run-up simulations with different computational methods for the Reynolds equation

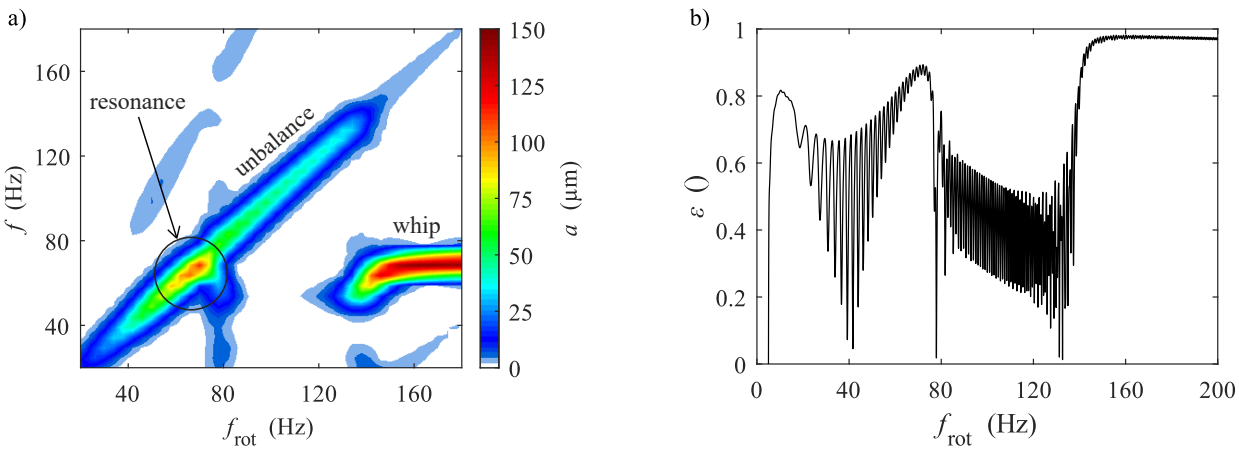

Fig. 3. Simulation results obtained with the SBFEM for a circumferential node number of $n_\theta = 480$. a) Spectrogram of the vertical shaft oscillations inside the bearing with amplitude a, frequency f, and rotational frequency f_{rot}. b) Relative eccentricity ε

The latter depicts the relative eccentricity $\varepsilon = q/c$ (eccentricity relative to the radial clearance) over the course of the run-up. According to the spectrogram, the oscillations are at first dominated by synchronous vibrations, which are excited by the unbalance. The amplitudes of these vibrations peak between $f_{rot} = 60\,\text{Hz}$ and $f_{rot} = 80\,\text{Hz}$ due to the resonance frequency of the rotor[12]

$$f_{res} = \frac{\omega_{res}}{2\pi} = \frac{1}{2\pi}\sqrt{\omega_0^2 - 2\delta^2} = \frac{1}{2\pi}\sqrt{\frac{k}{\frac{1}{2}m_1} - 2\left(\frac{b}{2\cdot\frac{1}{2}m_1}\right)^2}$$
$$= \frac{1}{2\pi}\sqrt{\frac{2k}{m_1} - \frac{2b^2}{m_1^2}} = 71.174\,\text{Hz}. \tag{28}$$

Here, ω_0 is the undamped natural angular frequency and δ is the exponential decay rate. For $f_{rot} > 140\,\text{Hz}$, high-amplitude subharmonic vibrations are observed that largely suppress the synchronous ones. These vibrations are caused by an oil whirl (self-excited vibration of the oil film) that resonates with the rotor (again due to f_{res}) and thereby leads to a whip. In Fig. 3b, this region is characterized by an almost constant eccentricity close to 1, indicating that the shaft orbit in the bearing is nearly circular and concentric with the shell. Altogether, the simulation results show the typical high-amplitude nonlinear oscillations that usually motivate the accurate and efficient modeling of transient rotor- and hydrodynamic interactions. This leads to the conclusion that the given rotor system, despite its simplicity, provides a reasonable basis for the now following comparison of the different methods (SBFEM, FEM, and FVM) and discretizations.

As a simple criterion for evaluating to what extent the simulation results differ between the considered computational models, the eccentricity during the oil whip ε_{whip} is analyzed, which also represents the amplitude of the shaft oscillations inside the bearing. However, the fact that the shaft orbit is not perfectly circular and concentric with the shell leads to a slightly time-dependent eccentricity and, therefore, complicates the comparison between the simulations. Thus, for convenience, the aver-

[12]This calculation assumes that the rotor is fixed at its two ends (at the bearings), which is why m_2 is not included.

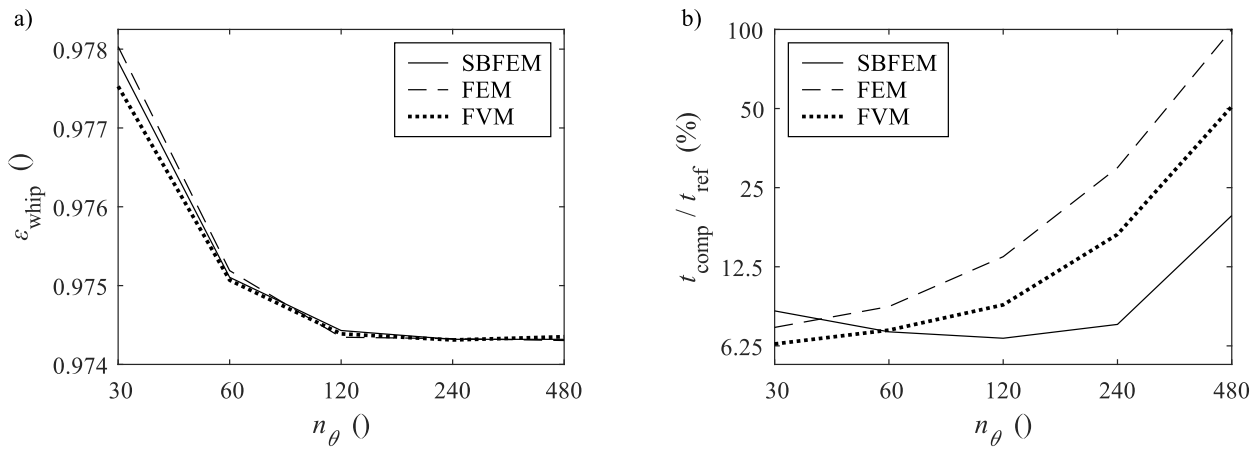

Fig. 4. Simulation results obtained with the SBFEM, FEM, and FVM for different circumferential node numbers n_θ. a) Average relative eccentricity during the oil whip ε_{whip}. b) Computational time t_{comp} relative to the maximum computational time t_{ref}

age eccentricity in the range from $f_{rot} = 160\,\text{Hz}$ to $f_{rot} = 198\,\text{Hz}$ is used. In Fig. 4a, ε_{whip} is depicted as a function of the circumferential node number n_θ for the SBFEM (solid lines), the FEM (dashed lines), and the FVM (dotted lines). The fact that the three curves are almost congruent is not surprising, since all computational methods have been implemented with linear interpolation functions (although in the SBFEM, this applies only to the circumferential direction) and, therefore, have a similar accuracy. It is observed that ε_{whip} converges over the mesh refinement steps and that the coarsest discretization ($n_\theta = 30$) already yields a quite small absolute error ($\Delta\varepsilon_{whip} \approx 0.003$). However, since the eccentricity is very close to 1 ($\varepsilon_{whip} \approx 0.9743$ for $n_\theta = 480$), this error reduces the minimum gap width $H_{min} = 1 - \varepsilon$ by about 12%, which might be critical in some cases. Thus, a node number of $n_\theta = 120$ or at least $n_\theta = 60$ should be used ($n_\theta = 100 \ldots 120$ is typical for rotordynamic simulations).

In Fig. 4b, the computational time required for the simulations t_{comp} is depicted (with logarithmic axis scaling) relative to a reference value ($t_{ref} = 17982\,\text{s}$) that corresponds to the most numerically expensive simulation (FEM with $n_\theta = 480$). For node numbers above $n_\theta = 60$, the fastest simulation is achieved with the SBFEM, followed by the FVM. Below $n_\theta = 60$, the FVM is the most efficient method. For the SBFEM, the computational time increases if the node number is reduced from 120 to 60 or from 60 to 30, which is surprising. The reason could be that the inaccurate computation of the bearing forces for coarse discretizations leads to an overestimation of the eccentricity (cf. Fig. 4a) and, thus, to a stiffer system. As a result, the ODE-solver has to reduce its step size and increase the number of time steps[13]. In case of the FEM and FVM, this effect is outweighed by the reduction of computational effort per time step. As already observed in previous studies [19], the SBFEM is comparatively inefficient for very coarse discretizations[14]. Altogether, under consideration of the computational effort as well as the accuracy, the SBFEM model with $n_\theta = 120$ is the most suitable of the investigated models.

For all considered node numbers, the FVM is significantly faster than the FEM, which has a simple explanation. In the FVM, every equation of the overall equation system (27) describes the interaction between a node 0 and the four respective neighboring nodes N, E, S, and W (cf. equation (26)). Hence, every row of the resulting matrix $\underline{\underline{K}}$ has five nonzero entries[15], except for those that are influenced by Dirichlet BCs. In the FEM model, every node directly interacts with the nodes of all four elements that it is part of. Thus, in contrast to the FVM, the four neighboring nodes in the diagonal directions are included as well, leading to nine nonzero entries per matrix row. In Fig. 5, the resulting matrix band structures are illustrated exemplarily for a small circumferential node number ($n_\theta = 15$). Here, the FEM (a) has 315 nonzero entries while the FVM (b) has only 195 and a smaller bandwidth. Due to these differences, the FEM requires more computational effort than the FVM for the solution of the equation system. It should be noted that the FEM element matrix (equation (20)) has been integrated analytically in this study, while in general, numerical quadrature techniques are also very common. The direct interaction between diagonally opposite nodes of the quadrilateral element can be avoided if Gauss-Lobatto-Legendre (GLL) quadrature [31] is used, where integration points are defined exactly at the nodes. In that case, the band structure in the FEM matrix is the same as in the FVM (Fig. 5b).

[13] Since ε_{whip} is quite large in all conducted simulations, the effect of the eccentricity on the bearing stiffness (large eccentricity leads to high stiffness) and the resulting step size (high stiffness requires small step size) also explains why the computational times, overall, are higher than one might expect for such a simple system.

[14] More specifically, the eigenvalue problem (SBFEM) is relatively expensive in comparison to the linear equation systems (FEM and FVM) under these conditions.

[15] Since the dependent variable (pressure P) is physically scalar, each node has only one degree of freedom.

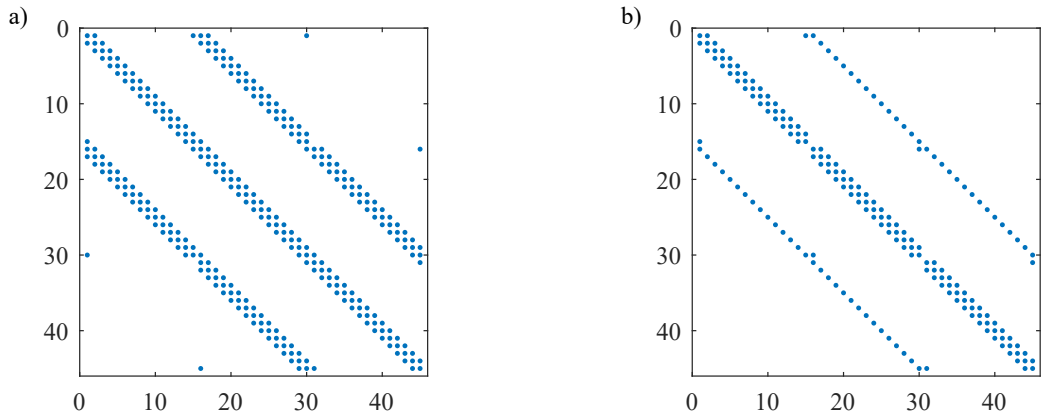

Fig. 5. Matrix band structure for an exemplary, coarse discretization of $n_\theta = 15$ nodes in the circumferential direction. a) FEM matrix with 315 nonzero entries. b) FVM matrix with 195 nonzero entries

4. CONCLUSIONS

In this study, a semi-analytical solution of the Reynolds equation, based on the SBFEM, is compared to the FEM and the FVM for the simulation of a Laval rotor with hydrodynamic bearings. For a circumferential node number of $n_\theta = 120$, all three investigated methods are accurate and the SBFEM is the computationally most efficient one. For finer discretizations, the relative efficiency of the SBFEM improves further, whereas for very coarse ones ($n_\theta < 60$), the FVM is faster than the SBFEM. The FEM is less efficient than the FVM for all investigated discretizations because its matrix has more nonzero entries and a larger bandwidth.

In future studies, similar investigations will be conducted for higher-order shape functions and with rotordynamic models of realistic technical systems. Since the pressure field may contain very high gradients in the minimum-gap region (in case of a large eccentricity) while remaining relatively smooth everywhere else, an adaptive discretization will be incorporated into the SBFEM solution for further improvement of the numerical efficiency. The SBFEM model with cavitation [21], which was not used in the study at hand, will be developed further and investigated in rotordynamic simulations as well. Moreover, the SBFEM will be compared to the look-up table approach.

ACKNOWLEDGEMENTS

The presented work is part of the project "Improvement of the numerical efficiency of rotordynamic simulations by application of the scaled boundary finite element method for the computation of hydrodynamic bearings", which is financially supported by the German Research Foundation (DFG) (project no. 490625563, grant no. WO 2085/8-1). This support is gratefully acknowledged.

REFERENCES

[1] B. Schweizer, "Oil whirl, oil whip and whirl/whip synchronization occurring in rotor systems with full-floating ring bearings," *Nonlinear Dyn.*, vol. 57, no. 4, pp. 509–532, 2009.

[2] E. Woschke, C. Daniel, and S. Nitzschke, "Excitation mechanisms of non-linear rotor systems with floating ring bearings – simulation and validation," *Int. J. Mech. Sci.*, vol. 134, pp. 15–27, 2017.

[3] O. Reynolds, "On the theory of lubrication and its application to Mr. Beauchamp Tower's experiments, including an experimental determination of the viscosity of olive oil," *Philos. Trans. R. Soc. Lond.*, vol. 177, pp. 157–234, 1886.

[4] A. Sommerfeld, "The hydrodynamic theory of lubrication friction," *Z. Math. Phys.*, vol. 50, no. 1-2, pp. 97–155, 1904.

[5] F.W. Ocvirk, "Short-bearing approximation for full journal bearings," National Advisory Committee for Aeronautics, Tech. Rep. 2808, 1952.

[6] M.M. Reddi, "Finite-element solution of the incompressible lubrication problem," *J. Lubr. Technol.*, vol. 91, no. 3, pp. 524–533, 07 1969, doi: 10.1115/1.3554977.

[7] K.H. Huebner, D.L. Dewhirst, D.E. Smith, and T.G. Byrom, *The Finite Element Method for Engineers*. John Wiley & Sons, 2001.

[8] M. Arghir, A. Alsayed, and D. Nicolas, "The finite volume solution of the Reynolds equation of lubrication with film discontinuities," *Int. J. Mech. Sci.*, vol. 44, no. 10, pp. 2119–2132, 2002.

[9] W.M. Dmochowski, A. Dadouche, and M. Fillon, *Finite difference method for fluid-film bearings*. Boston, MA: Springer US, 2013, pp. 1137–1143.

[10] B. Schweizer, "Total instability of turbocharger rotors – physical explanation of the dynamic failure of rotors with full-floating ring bearings," *J. Sound Vibr.*, vol. 328, no. 1-2, pp. 156–190, 2009.

[11] A. Chasalevris, P. Nikolakopoulos, and C. Papadopoulos, "Aligned and misaligned wear pattern in fluid film bearings and influence on the rotor response," in *Proceedings of the 9th International Conference on Vibrations in Rotating Machines SIRM*, 2011.

[12] R. Eling, M. Te Wierik, R. Van Ostayen, and D. Rixen, "Towards accurate prediction of unbalance response, oil whirl and oil whip of flexible rotors supported by hydrodynamic bearings," *Lubricants*, vol. 4, no. 3, p. 33, 2016.

[13] H.G. Elrod, "A cavitation algorithm," *J. Lubr. Technol.*, vol. 103, no. 3, pp. 350–354, 07 1981, doi: 10.1115/1.3251669.

[14] N.S. Feng and E.J. Hahn, "Density and viscosity models for two-phase homogeneous hydrodynamic damper fluids," *ASLE Trans.*, vol. 29, no. 3, pp. 361–369, 1986.

[15] J.F. Booker and S. Boedo, "Finite element analysis of elastic engine bearing lubrication: theory," *Revue Européenne des Éléments Finis*, vol. 10, no. 6-7, pp. 705–724, 2001.

[16] S. Boedo and J.F. Booker, "Finite element analysis of elastic engine bearing lubrication: application," *Revue Européenne des Éléments Finis*, vol. 10, no. 6-7, pp. 725–739, 2001.

[17] C. Irmscher, C. Ziese, M. Kreschel, and E. Woschke, "Run-up simulation of an automotive turbocharger rotor using an extensive thermo-hydrodynamic bearing model," in *SIRM 2021 – 14th International Conference on Dynamics of Rotating Machines*, G. Żywica and T. Szolc, Eds., Institute of Fluid Flow Machinery, Polish Academy of Sciences. Gdańsk, Poland: IMP PAN Publishers, 2021, pp. 145–155.

[18] E. Woschke, C. Daniel, S. Nitzschke, and J. Strackeljan, "Numerical run-up simulation of a turbocharger with full floating ring bearings," in *Vibration Problems ICOVP 2011: the 10th International Conference on Vibration Problems*. ICOVP 2011 Supplement, 2011, p. 334.

[19] S. Pfeil, H. Gravenkamp, F. Duvigneau, and E. Woschke, "Scaled boundary finite element method for hydrodynamic bearings in rotordynamic simulations," *Int. J. Mech. Sci.*, vol. 199, p. 106427, 2021.

[20] S. Pfeil, H. Gravenkamp, F. Duvigneau, and E. Woschke, "High-order SBFEM solution of the Reynolds equation," in *Proceedings in Applied Mathematics and Mechanics*, vol. 21. Wiley Online Library, 2021, doi: 10.1002/pamm.202100028.

[21] S. Pfeil, H. Gravenkamp, F. Duvigneau, and E. Woschke, "Semi-analytical solution of the Reynolds equation considering cavitation," *Int. J. Mech. Sci.*, vol. 247, p. 108164, 2023, doi: 10.1016/j.ijmecsci.2023.108164.

[22] J.P. Wolf and C. Song, "Consistent infinitesimal finite-element cell method: in-plane motion," *Comput. Meth. Appl. Mech. Eng.*, vol. 123, no. 1-4, pp. 355–370, 1995.

[23] C. Song and J.P. Wolf, "Consistent infinitesimal finite-element cell method: out-of-plane motion," *J. Eng. Mech.*, vol. 121, no. 5, pp. 613–619, 1995.

[24] I. Chiong, E.T. Ooi, C. Song, and F. Tin-Loi, "Scaled boundary polygons with application to fracture analysis of functionally graded materials," *Int. J. Numer. Methods Eng.*, vol. 98, no. 8, pp. 562–589, 2014.

[25] C. Song and J.P. Wolf, "Semi-analytical representation of stress singularities as occurring in cracks in anisotropic multi-materials with the scaled boundary finite-element method," *Comput. Struct.*, vol. 80, no. 2, pp. 183–197, 2002.

[26] Y. Hori, *Hydrodynamic Lubrication*. Springer Science & Business Media, 2006.

[27] L.F. Shampine, M.W. Reichelt, and J.A. Kierzenka, "Solving index-1 DAEs in MATLAB and Simulink," *SIAM Rev.*, vol. 41, no. 3, pp. 538–552, 1999, doi: 10.1137/S003614459933425X.

[28] M. Okereke and S. Keates, "Finite element applications," *Cham: Springer International Publishing AG*, 2018.

[29] F. Moukalled, L. Mangani, and M. Darwish, *The Discretization Process*. Cham: Springer International Publishing, 2016, pp. 85–101.

[30] N.J. Higham, "Cholesky factorization," *WIREs Comput. Stat.*, vol. 1, no. 2, pp. 251–254, 2009, doi: 10.1002/wics.18.

[31] F.B. Hildebrand, *Introduction to Numerical Analysis: Second Edition*, ser. Dover Books on Mathematics. Dover Publications, 2013.